photonics

MDPI

Article

Ultrafast Nonequilibrium Carrier Dynamics in Topological Insulator Bi_2Se_3 Probed by Terahertz Spectroscopy at Room Temperature

Nuoxi Yu [1,†], Zhiqiang Lan [1,†], Tianhui Wang [1], Yuanyuan Guo [1], Changwei Li [1], Kaijie Chen [1], Yinwei Li [1], Yinghao Yuan [1,*] and Zuanming Jin [1,2,*]

[1] Shanghai Key Lab of Modern Optical System, Terahertz Technology Innovation Research Institute, Terahertz Spectrum and Imaging Technology Cooperative Innovation Center, University of Shanghai for Science and Technology, Shanghai 200093, China; 2335060308@st.usst.edu.cn (N.Y.); 241200078@st.usst.edu.cu (Z.L.); 243350582@st.usst.edu.cn (T.W.); 255340620@st.usst.edu.cn (Y.G.); 2335051115@st.usst.edu.cn (C.L.); 2235061508@st.usst.edu.cu (K.C.); liyw@usst.edu.cn (Y.L.)

[2] Shanghai Institute of Intelligent Science and Technology, Tongji University, Shanghai 200092, China

* Correspondence: yhyuan@usst.edu.cn (Y.Y.); physics_jzm@usst.edu.cn (Z.J.)

† These authors contributed equally to this work.

Abstract

Topological insulators (TIs) feature unique Dirac fermion-hosting surface states with exceptional electronic properties, rendering them promising candidates for optoelectronic and spintronic applications. Herein, we investigate the relaxation dynamics of photoexcited carriers in Bi_2Se_3 films via optical pump–terahertz (THz) probe spectroscopy (OPTP) at room temperature. Under 800 nm pump pulse excitation, the time-dependent real part of the pump excitation conductivity $\Delta\sigma$ exhibits a positive-to-negative sign reversal as carriers relax toward equilibrium, which is further validated by frequency-dependent conductivity spectra at varied pump-probe delays. The initial positive $\Delta\sigma$ originates dominantly from bulk carrier contributions, while the negative component at prolonged delays is ascribed to Dirac surface states, driven by enhanced scattering of photoexcited carriers. Using the Drude–Smith model to fit the differential conductivity spectra, we quantitatively extracted time-dependent transport parameters of bulk and surface states. These results unravel the comprehensive carrier relaxation mechanism in Bi_2Se_3, clarify the distinct roles of surface and bulk contributions, and lay the groundwork for designing TI-based THz devices.

Keywords: Bi_2Se_3 thin films; ultrafast carriers dynamics; conductivity; Drude–Smith model

1. Introduction

Topological insulators (TIs) are a unique class of quantum matter, exhibiting insulating properties in their bulk states while maintaining metallic or conductive electronic states at the surface or edge, protected by time-reversal symmetry [1–5]. These topological edge states exhibit linearly dispersive Dirac-type band structures and possess spin-momentum locking properties, which endow them with significant application prospects in spintronics and low-power devices [6–10]. In addition, the TI's properties have been demonstrated to obtain surface currents associated with spin polarization, providing a potential platform for novel opto-spintronic devices.

Recently, three-dimensional TIs, including bismuth selenide (Bi_2Se_3), antimony telluride (Sb_2Te_3), and bismuth telluride (Bi_2Te_3), have drawn considerable attention because

Check for updates

Received: 15 March 2026
Revised: 14 April 2026
Accepted: 14 April 2026
Published: 15 April 2026

Copyright: © 2026 by the authors. Licensee MDPI, Basel, Switzerland. This article is an open access article distributed under the terms and conditions of the Creative Commons Attribution (CC BY) license.

their properties differ markedly from those of conventional semiconductors and insulators [11–14]. These materials show an electronic band structure where gapless surface states, protected by topology, exist alongside bulk states with a semiconductor band gap [15,16]. The surface states exhibit a linear electronic dispersion near the charge neutrality point, analogous to Dirac fermions in graphene. This characteristic gives it outstanding properties suitable for a range of spintronic and optoelectronic devices, such as broadband near-infrared THz modulators and photodetectors [17–20]. The demand for rapid response times in such device applications renders it critical to investigate the different scattering pathways involved in the relaxation process of hot carriers [21–25].

Femtosecond-resolved ultrafast lasers have enabled the investigation of near- and far-from-equilibrium processes in condensed matter systems, facilitating deeper insight into the temporal behavior of topological states [26–32]. Since Bi_2Se_3 was predicted to be a topological insulator nearly two decades ago, it has been extensively investigated through both experimental and theoretical studies. A wide range of experimental techniques, including terahertz, infrared, and visible light spectroscopies, have been applied to explore its properties. THz time-domain spectroscopy (TDS) studies have revealed surface-state-dominated metallic transport in Bi_2Se_3 at low temperatures (<30 K), enabling separation of topological surface and bulk contributions [33]. Optical pump optical probe spectroscopy (OPOP) [34,35] revealed bulk and surface carrier dynamics in Bi_2Se_3. For example, near-infrared pump–mid-infrared probe spectroscopy was used to probe intervalley scattering and its nonlinear evolution [36]. Femtosecond transient absorption spectroscopy was used to demonstrate distinct bulk and surface dynamics, with fast bulk band filling and delayed surface-state population mediated by carrier–phonon scattering [37]. Time-resolved angle-resolved photoemission spectroscopy (tr-ARPES) demonstrated that electron–phonon scattering is the dominant mechanism underlying carrier relaxation in photoexcited Bi_2Se_3 [38–40]. Ultrafast magneto-optical Kerr effect measurements further capture the spin dynamics coupled with Dirac surface states, providing direct evidence for understanding the non-equilibrium evolution in spin–orbit coupling systems [41,42]. The THz high-harmonic generation (HHG) spectroscopy was employed to study the Bi_2Se_3 and $(Bi_{0.9}In_{0.1})_2Se_3$, revealing that the observed THz HHG signal originates from the surface states [43,44]. Nevertheless, OPOP mainly responds to the interband transitions; tr-ARPES suffers from limited spectral resolution around the Fermi level and primarily probes surface carriers. Therefore, these measurements generally cannot unambiguously distinguish contributions from bulk and surface carriers.

In the study of non-equilibrium dynamics, optical pump–THz probe spectroscopy (OPTP) enables investigation of free-carrier dynamics relevant to transport properties, and its deep penetration allows it to probe both bulk and surface carriers [45,46]. This technique is particularly effective for studying materials hosting Dirac fermions, as demonstrated by prior investigations on graphene carrier dynamics under photoexcitation [47,48]. The selective excitation of specific band transitions in TIs using THz optical pulses, combined with THz detection techniques to monitor low-energy excitation processes, can distinguish the dynamic responses of bulk states from surface states [49].

Using OPTP, Sangwan Sim et al. investigated Bi_2Se_3 films ranging from 5 to 32 quintuple layers (QL, 1 QL = 0.9 nm) in thickness, observing that the real part of photoconductivity ($\Delta\sigma$) exhibits a negative value in 5 QL films and a positive value in 32 QL films [21]. The temporal dynamics of $\Delta\sigma$ with respect to the optical pumping and THz probing also reflect this physical phenomenon [11,50]. While these studies have established an important foundation for understanding ultrafast carrier dynamics in Bi_2Se_3, particularly under low-temperature conditions [50], the corresponding behavior at room temperature remains less explored. In particular, the temporal evolution of the photoconductivity sign changes

following photoexcitation, as well as the respective contributions from bulk and surface states, are still not fully understood in thin-film systems under ambient conditions. Given that room-temperature operation is crucial for practical optoelectronic applications, it is essential to investigate the pump fluence-dependent ultrafast conductivity dynamics. In this work, we demonstrate that optical pump fluence-dependent OPTP experiments performed on Bi_2Se_3 thin films enable quantitative evaluation of the individual and combined impacts of surface and bulk states on photoexcited carrier dynamics in TIs at room temperature. The differential THz conductivity $\Delta\sigma$ obtained in our experiments exhibits a positive-to-negative sign reversal with increasing pump-probe time delay. The observed sign reversal of $\Delta\sigma$ reflects the synergistic contributions from the semiconducting bulk states and metallic surface states in Bi_2Se_3.

2. Materials and Methods

2.1. Sample Preparation

Bi_2Se_3 thin films were grown with 0.3 g of 99.995% pure Bi_2O_3 powder serving as the bismuth source and 2 g of 99.999% high-purity Se granules as the selenium source, while argon (Ar) and hydrogen (H_2) at flow rates of 200 sccm and 15 sccm respectively, were utilized as carrier gases. A dual-temperature-zone tube furnace was adopted for the growth process, with Bi_2O_3 positioned in the high-temperature zone heated to 700 °C and Se placed in the low-temperature zone held at 300 °C. Al_2O_3 sapphire substrates were positioned 5 cm downstream of the Bi_2O_3, where the temperature was approximately 500 °C. After 15 min of growth, roughly 20 QL of Bi_2Se_3 films were deposited on the substrates. The sample was purchased from Shenzhen 6Carbonn Technology Co., Ltd. (Shenzhen, China).

2.2. Experimental Setup

OPTP measurements in this work were conducted with a self-constructed experimental setup, as schematically depicted in Figure 1a. We adopted an amplified Ti:sapphire laser system as the excitation light source, which produces laser pulses with a wavelength of 800 nm (1.55 eV), a pulse duration of 120 fs, and a repetition rate of 1 kHz. The laser beam was split into three separate beams: a pump beam for optically exciting the sample, a generation beam that generates terahertz radiation through optical rectification in a <110> ZnTe crystal, and a gating beam for electro-optic detection of THz signals in another <110> ZnTe crystal. The pump beam was chopped at a frequency of 500 Hz, and the resulting signal was output by a balanced photodiode and fed into a lock-in amplifier. Inserting the optical chopper into the THz generation beam path allows for the measurement of frequency-resolved THz spectra (chopper 1 in the figure) by adjusting the position of delay stage 2 (t_s). In addition, the chopper can be placed into the pump beam path to detect the frequency-integrated and frequency-resolved photoinduced responses at different pump-probe delay times (t_p) (chopper 2 in the figure). The pump fluence was adjusted using neutral density filters to range from 0.05 to 1.0 mJ/cm^2. The pump beam and the THz beam were both linearly polarized, with their polarization directions kept parallel to each other. Dry air was purged through the entire setup during the experiments to suppress water vapor absorption, maintaining the relative humidity below 10%.

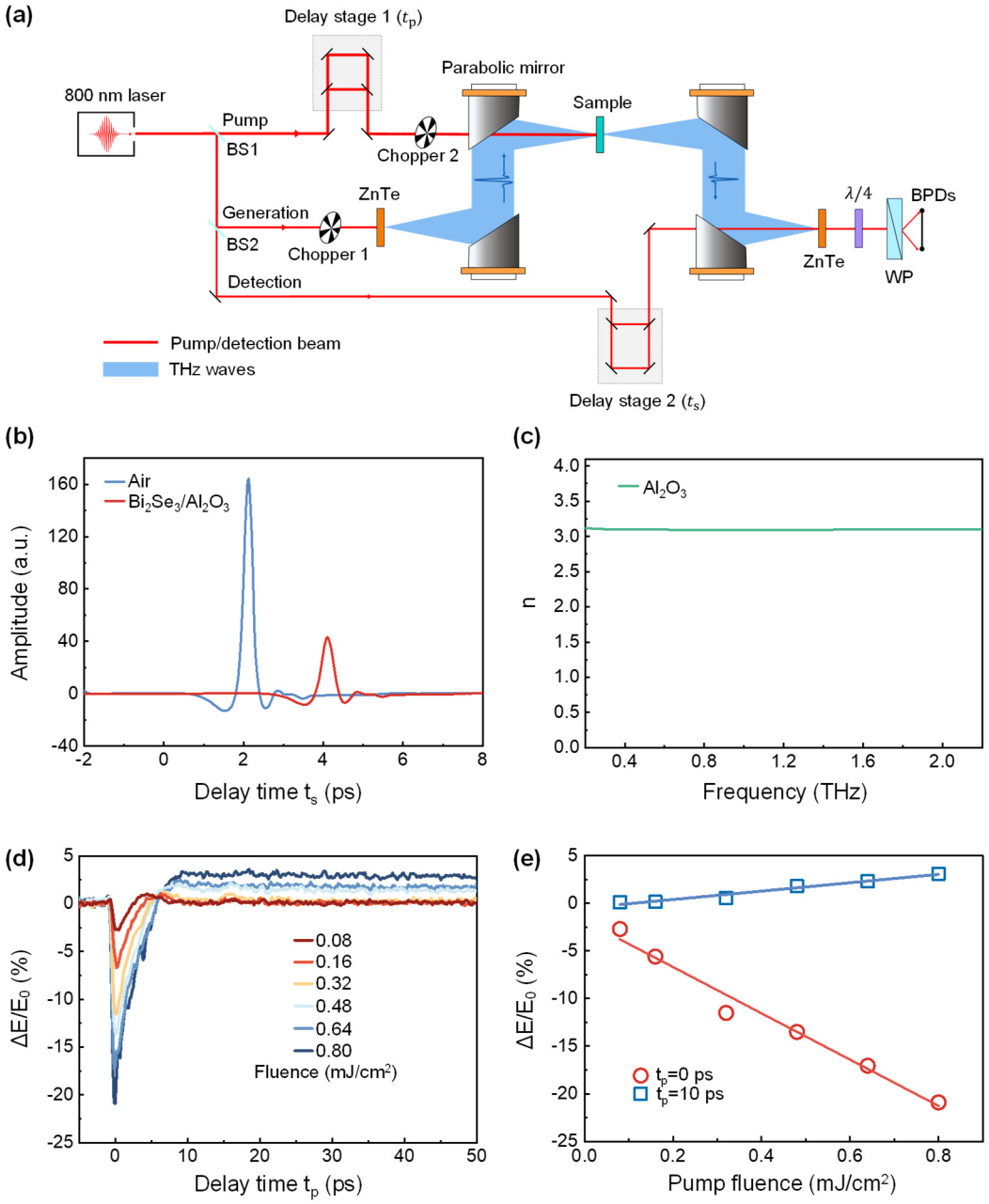


Figure 1. (**a**) Schematic diagram of the OPTP experimental setup. The red line represents the propagation of the pump/detection light, and the blue area is the THz wave. BS1 and BS2: beam splitters; λ/2: half-wave plate; chopper: optical chopper; λ/4: quarter-wave plate; WP: Wollaston prism; BPDs: balanced photodiodes. (**b**) THz transmission time-domain spectral signal of the air (blue line) and the Bi_2Se_3 film on Al_2O_3 substrate (red line), respectively. (**c**) Refractive index of Al_2O_3 substrate in the THz range of 0.2–2.2 THz. (**d**) THz transmittance ($\Delta E/E_0$) plotted against the delay time for a series of different pump fluences. (**e**) The values of $\Delta E/E_0$ at pump-probe delays of t_p = 0 ps (red) and t_p = 10 ps (blue) plotted as a function of pump fluence, where the solid lines stand for the linear fitting results.

3. Results and Discussion

We performed OPTP measurements on the 20 QL Bi_2Se_3 thin film. Figure 1b shows the THz electric fields transmitted through air and Bi_2Se_3 thin films on an Al_2O_3 substrate without pump light excitation. Figure 1c shows that the refractive index of the Al_2O_3 substrate is n = 3.09 in the THz range; this is consistent with that reported in the literature [51]. Figure 1d shows the normalized transient THz transmission $\Delta E/E_0$ acquired

under different pump fluence conditions. It is worth noting that $\Delta E = E_{Pump} - E_0$ stands for the pump-induced variation in THz transmission amplitude. Specifically, E_0 and E_{Pump} represent the peak values of the THz transmission waveform in the absence and presence of the pump beam, respectively. In the initial several picoseconds (≈5–7 ps), the $\Delta E/E_0$ value is negative, which is manifested as a sharp drop. Subsequently, the THz transmission in the Bi_2Se_3 film rises and changes from negative to positive. Figure 1e depicts the variation in $\Delta E/E_0$ with pump fluence at the pump-probe delay times of t_p = 0 ps and t_p = 10 ps. The negative $\Delta E/E_0$ signal at t_p = 0 ps declines with the increase in pump fluence, whereas the positive $\Delta E/E_0$ signal at t_p = 10 ps exhibits a linear increase as the pump fluence rises. A negative $\Delta E/E_0$ value is indicative of enhanced absorption of the THz electric field by the sample, a phenomenon defined as photoinduced absorption; in contrast, a positive $\Delta E/E_0$ value denotes a reduction in such absorption, which is referred to as photoinduced bleaching. In contrast to conventional semiconductor materials, this unusual transparency can be ascribed to the metallic behavior of the topological surface state (TSS) [52]. At a pump fluence of 0.8 mJ/cm^2, this material exhibits prominent THz switching performance, achieving a modulation depth of more than 20%. A positive linear correlation is observed between the modulation depth and pump fluence, and no saturation phenomenon appears within the tested pump fluence range. This result implies that the modulation depth can be further improved by applying more intense optical excitation.

To further analyze the dynamic relaxation processes of nonequilibrium carriers in the Bi_2Se_3 thin film upon photoexcitation, we calculated the THz sheet conductivity using the following relation [53,54]:

$$\Delta\sigma = \frac{1+n}{Z_0}\left(\frac{1}{1+\Delta E/E_0} - 1\right), \quad (1)$$

where n = 3.09 represents the refractive index of the Al_2O_3 substrate in the THz range, and Z_0 = 377 Ω stands for the characteristic impedance of free space. Figure 2a illustrates the photoinduced THz conductivity of the sample under different pump fluences ranging from 0.08 to 0.80 mJ/cm^2. The observed sign reversal of $\Delta\sigma$ from positive to negative directly reflects the combined effects of carrier density and scattering rate in both the surface and bulk states of this topological material. We find that the ultrafast dynamic evolution of $\Delta\sigma$ at short time scales is dominated by bulk carriers, with the subsequent carrier relaxation process governed by the metallic topological surface states; this result is consistent with the conclusions of previous studies on Bi_2Se_3 [11]. Figure 2b presents the dependence of the delay time t_p at $\Delta\sigma$ = 0 on the different pump fluences. As the pump fluence increases, the corresponding t_p also increases, from 2.48 ps at 0.08 mJ/cm^2 to 6.82 ps at 0.80 mJ/cm^2. This indicates that, with increasing pump fluence, the Bi_2Se_3 film requires a longer time to complete the transition from positive to negative conductivity.

Qualitatively, this photoconductivity can be interpreted within the framework of the Drude model, $\sigma(\omega) = \frac{D}{\Gamma - i\omega}$, where D is the Drude weight and Γ is the average momentum scattering rate of the charge carriers. The photoinduced variation in the real component of the photoconductivity can be expressed $\frac{\Delta\sigma}{\sigma} = \frac{\Delta D}{D} - \frac{\Delta\Gamma}{\Gamma}$. In the semiconducting bulk state of TIs, photoexcitation gives rise to an increase in carrier density, thereby rendering $\Delta D > 0$. For the metallic topological surface states, upon optical pulse excitation, the temperature of the electronic system rises, leading to an increased hot carrier scattering rate that far exceeds the increment in carrier density, resulting in $\Delta\Gamma > 0$ and potentially leading to a negative value of the photoconductivity $\Delta\sigma$ [55,56].

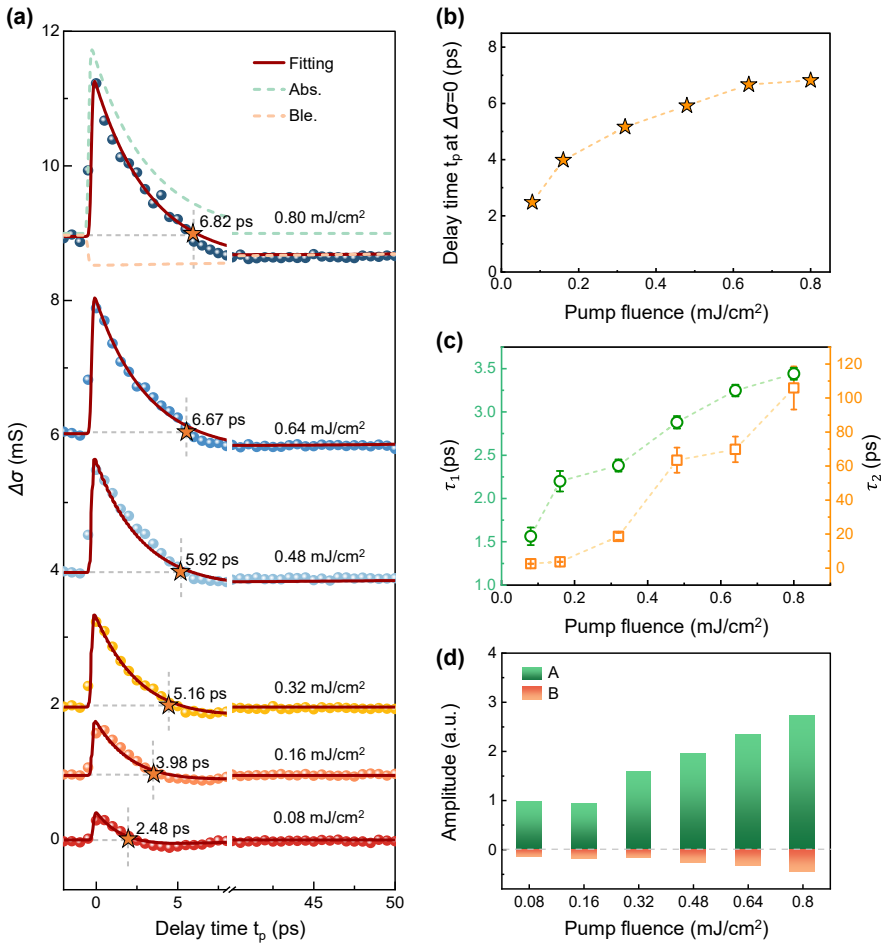


Figure 2. (**a**) Photoexcited THz conductivity in Bi_2Se_3 film under different pump fluences. The red solid line is fitted using the Equation (2). While the green and orange dashed lines correspond to the positive conductivity (photoinduced absorption) and negative conductivity (photoinduced bleaching) components, respectively. The pentagram markers denote the pump–probe delay time t_p corresponding to $\Delta\sigma = 0$. (**b**) The dependence of the pump–probe delay time t_p, corresponding to $\Delta\sigma = 0$ on the pump fluence. (**c**) Pump fluence-dependent relaxation times τ_1 and τ_2, corresponding to the bulk and surface state relaxation times, respectively. (**d**) The coefficients A and B plotted as a function of pump fluence.

Quantitatively, the relaxation behavior of the transient THz conductivity can be understood using a bi-exponential relaxation function convolved with the laser pulse [57],

$$\begin{aligned}\Delta\sigma(t_p) = Ae^{-\left(\frac{t_p}{\tau_1}-\frac{\omega^2}{\tau_1{}^2}\right)} \times \left[1-\mathrm{erf}\left(\frac{\omega}{\tau_1}-\frac{t_p}{2\omega}\right)\right] \\ +Be^{-\left(\frac{t_p}{\tau_2}-\frac{\omega^2}{\tau_2{}^2}\right)} \times \left[1-\mathrm{erf}\left(\frac{\omega}{\tau_2}-\frac{t_p}{2\omega}\right)\right]\end{aligned} \quad (2)$$

where t_p is the pump-probe time delay, and ω is the full width at half maximum (FWHM) of the THz pulse. The exponential relaxation of positive $\Delta\sigma$ (first term) corresponds to carrier relaxation in the conduction band of the bulk states. This second term accounts for the exponential decay of negative $\Delta\sigma$, corresponding to the carrier interband scattering process within the TSS and electron-hole recombination. The coefficients A and B relate to the relaxation channels of the bulk and TSS, respectively, and τ_1 and τ_2 represent the associated relaxation time constants for these channels.

As depicted in Figure 2c, the τ_1 corresponding to the positive photoconductivity increases from 1.5 ps to 3.4 ps owing to electron-phonon coupling, which confirms the ultrafast switching performance of TI-based devices. In the region dominated by topological

surface states (TSS), the carrier recombination process has a much longer time scale, and the relaxation time τ_2 related to negative photoconductivity rises from 2.5 ps to 105 ps with the pump fluence increasing from 0.08 to 0.80 mJ/cm^2. As shown in Figure 2d, the fitting coefficients A and B, associated with the bulk and surface states, rise as the pump fluence increases.

Figure 3a,b shows schematic of the electron distribution in Bi_2Se_3 upon excitation by linearly polarized pulses. The band structure of Bi_2Se_3 near the Fermi level is relatively simple, with a bulk band gap of about 0.3 eV. Within this band gap, a topologically protected Dirac surface state is present, which bridges the conduction band and the valence band of the material. The observed sign reversal of $\Delta\sigma$ originates from the synergistic contributions of charge carriers in the bulk and surface electronic states.

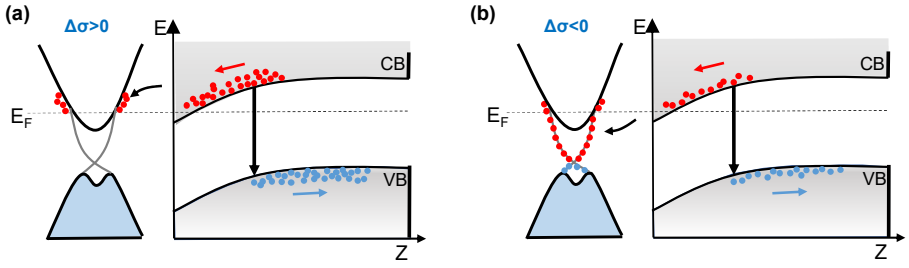


Figure 3. Diagrammatic representation of (**a**) bulk and (**b**) surface state contribution to $\Delta\sigma$. Solid red dots and blue dots represent electrons and holes, respectively. The red arrows indicate the transport direction of electrons, the blue arrows indicate the transport direction of holes, the short black arrows represent the transfer from bulk states to surface states, and the long black arrows represent electron–hole recombination within the bulk states.

An 800 nm pump laser (with a photon energy of ~1.55 eV) delivers ample energy to enable carriers to transfer from the bulk valence band to the bulk conduction band. The hot electrons primarily occupy the unoccupied regions of the bulk conduction band. Within several hundred femtoseconds, electron–electron scattering drives electrons into a non-equilibrium Fermi–Dirac distribution, strengthening free-carrier THz absorption and causing a rapid rise in positive $\Delta\sigma$ immediately after photoexcitation. Hot carriers initially dissipate their energy to the lattice through intraband transitions and accumulate at the bottom of the lower bulk conduction band, prior to being injected into the linear band structure of the TSS. This process elevates scattering and reduces carrier mobility in the TSS, ultimately yielding negative $\Delta\sigma$.

The long-lived negative photoconductivity observed several picoseconds post-photoexcitation signifies the major contribution originating from surface state carriers to the THz photoconductivity at longer delay times. We propose that enhanced surface state carrier scattering may account for the observed positive relationship between the relaxation time τ_2 and pump fluence in Bi_2Se_3 thin films. Thus, the observed phenomenon can be explained by the fact that the photoinduced variation in $\Delta\sigma$ for the 20 QL Bi_2Se_3 thin film stems from the circumstance that the vast majority of photoexcited carriers are initially situated in the bulk states, with a lifetime of merely several picoseconds prior to surface carriers emerging as the dominant factor governing THz transmission.

For an in-depth study of the transport properties of charge carriers, we further measured the THz time-domain transmission signals in the Bi_2Se_3 film upon photoexcitation. Figure 4a presents the terahertz time-domain waveforms for the sample in the absence of pump excitation (black curve), as well as the differential terahertz transmission signal $\Delta E(t)$ acquired at pump-probe delays of 0 ps and 7 ps following photoexcitation with pump fluences of 0.16, 0.32, and 0.64 mJ/cm^2.

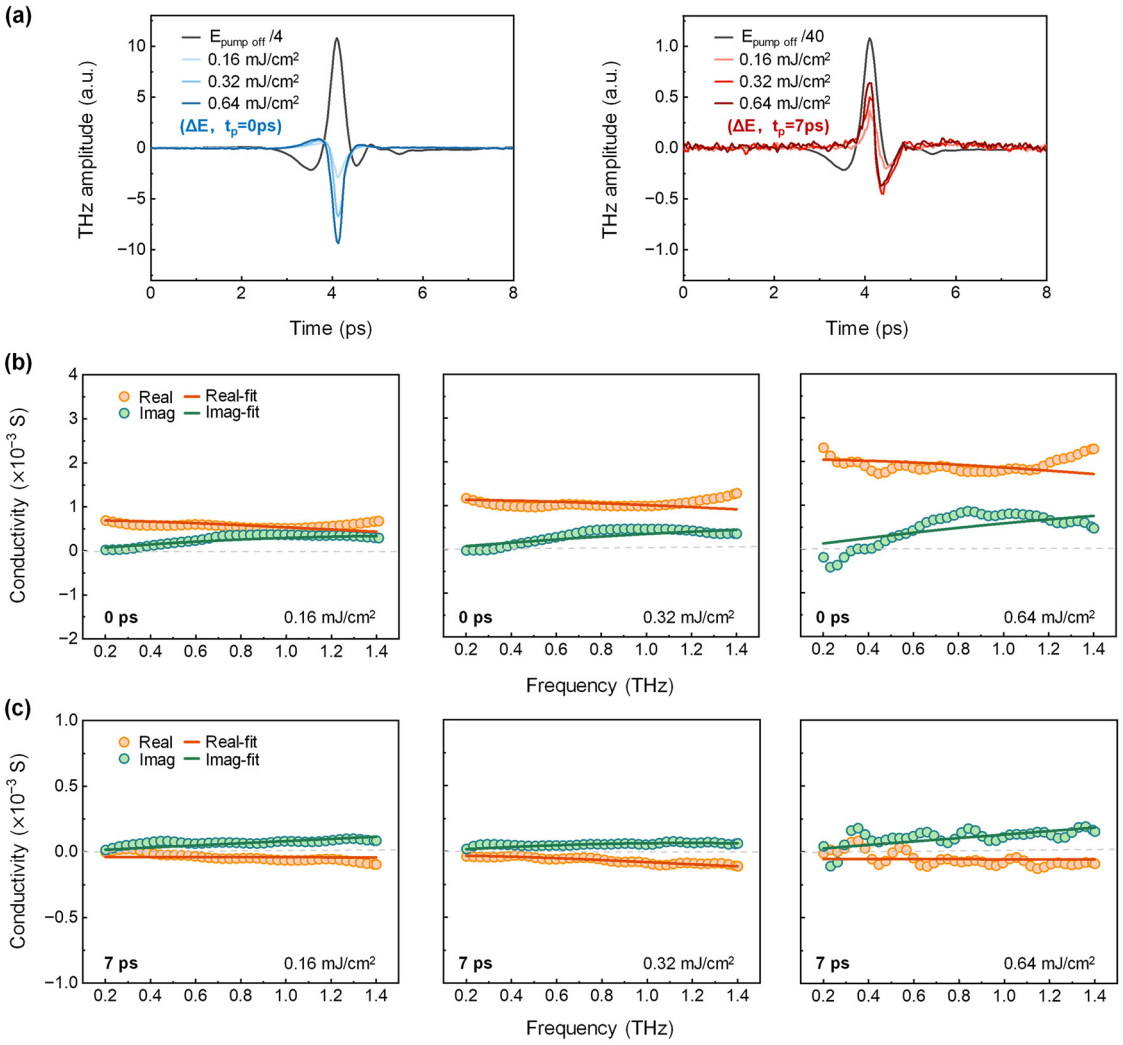


Figure 4. (**a**) THz transmission waveforms of the unexcited sample (black curve), along with those measured at pump fluences of 0.16 mJ/cm^2, 0.32 mJ/cm^2, and 0.64 mJ/cm^2 at pump-probe delay times of t_p = 0 ps (blue curve) and t_p = 7 ps (red curve), respectively. The real parts (plotted as orange circles) and imaginary components (plotted as green circles) of the THz-frequency conductivity spectra for Bi_2Se_3 thin films at pump-probe delay times t_p of 0 ps (panel (**b**)) and 7 ps (panel (**c**)) under varying pump fluences. The solid curves correspond to the fitted results derived from the Drude–Smith model. The dashed line represents zero conductivity.

Then, we extracted the complex conductivity in the THz frequency range $\tilde{\sigma}(\omega)$. The calculation of complex conductivity can be given by the following formula:

$$\sigma_{re} = \left(\frac{\cos\phi}{A} - 1\right)\frac{1+n}{(Z_0 l)} \tag{3}$$

$$\sigma_{im} = \frac{-(1+n)\sin\phi}{AZ_0 l} \tag{4}$$

where n stands for the refractive index of Al_2O_3 in the terahertz spectral range; l is the thickness of the sample. A and ϕ denote the amplitude ratio of the transmitted THz electric field for the substrate coated with the film relative to the uncoated substrate, and the corresponding phase difference between the two, respectively. Figure 4b,c show the real and imaginary parts of THz conductivity. $\tilde{\sigma}(\omega)$ at t_p = 0 ps and 7 ps under different

pump fluences. We analyzed the experimentally measured $\tilde{\sigma}(\omega)$ with the Drude–Smith model [58,59],

$$\tilde{\sigma}(\omega) = \frac{\sigma_{dc}}{1 - i\omega\tau}[1 + \frac{c}{1 - i\omega\tau}] \quad (5)$$

where σ_{dc} denotes the direct current conductivity and τ stands for the momentum scattering time. The parameter c, which takes values in the range of -1 to 0, is a phenomenological coefficient that quantifies the backscattering effect or restoring force, and thus characterizes the extent of carrier localization. As illustrated in Figure 4b,c, the orange solid curves represent the fitted results for $\sigma_{real}(\omega)$, while the green solid curves correspond to the fitted results for $\sigma_{imag}(\omega)$. The Drude–Smith (DS) model exhibits a good consistency with the experimental findings. As shown in Figure 4b, when t_p = 0 ps, the real part of conductivity increases with pump fluence, exhibiting positive photoconductivity. The σ_{dc} increases from 0.69×10^{-3} S at a pump fluence of 0.16 mJ/cm^2 to 2.05×10^{-3} S at 0.64 mJ/cm^2. In contrast, when t_p = 7 ps, as Figure 4c shows, the real part of conductivity is negative, which decreases slightly with pump fluence.

At the pump fluence of 0.16 mJ/cm^2, scattering time τ is 85.62 fs for the t_p = 0 ps, which is longer than τ = 56.56 fs for the t_p = 7 ps. It shows that with increasing time delay, the scattering time of hot electrons in the TSS decreases, raising the scattering rate and accounting for the negative sign of the real part of the conductivity at long delay times. On the other hand, for the t_p = 0 ps, c is close to 0 under the pump fluence ranging from 0.16 to 0.64 mJ/cm^2. In contrast, for the t_p = 7 ps, c is close to -0.97, which corresponds to a strong backscattering. Our results reveal that electrons exhibit different localization behaviors at two pump-probe time delays, primarily as a result of the differing scattering properties of bulk and surface states.

4. Conclusions

To conclude, this research probed the ultrafast electronic dynamics in Bi_2Se_3 using OPTP measurements at room temperature. Experimental findings indicate that photoexcitation with 1.55 eV photons mainly initiates excitation within the interior states, which in turn induces rapid carrier migration and subsequent reallocation toward the surface layer. This experimental approach allows for direct visualization of the vacant band structure and captures, with femtosecond temporal resolution, the distinct light-induced behaviors across different unoccupied bands. The unique coexistence of Dirac electronic states and semiconductor-like bulk states makes TIs promising candidates for developing low-cost, high-performance optically triggered ultrafast switches, as well as for realizing active control over terahertz wave propagation.

Author Contributions: Conceptualization, Z.L., Y.Y., and Z.J.; methodology, T.W., C.L., K.C., and Y.G.; formal analysis, N.Y., Z.L., and Y.L.; investigation, N.Y., Z.L., and K.C.; data curation, Z.L. and Y.G.; data review, Z.J.; writing—original draft preparation, N.Y., Z.L., and Z.J.; writing—review, Z.J. and Y.Y.; writing—editing, Z.J. and Y.Y. All authors have read and agreed to the published version of the manuscript.

Funding: This research was funded by the National Key Research and Development Program of China (2023YFF0719200); the National Natural Science Foundation of China (62322115, U24A20226, 62588201, 62435010, 62335012, 12274278); the 111 Project (Grant No. D18014); Shanghai Educational Development Foundation (24SG46); the key project supported by Science and Technology Commission Shanghai Municipality (YDZX20193100004960); the Science and Technology Commission of Shanghai Municipality (22JC1400200); and the General Administration of Customs People's Republic of China (2019HK006).

Data Availability Statement: The data presented in this study are available on request from the corresponding authors.

Conflicts of Interest: The authors declare no conflicts of interest.

References

1. Hasan, M.Z.; Kane, C.L. Colloquium: Topological insulators. *Rev. Mod. Phys.* **2010**, *82*, 3045–3067. [CrossRef]
2. Qi, X.L.; Zhang, S.C. Topological insulators and superconductors. *Rev. Mod. Phys.* **2011**, *83*, 1057–1110. [CrossRef]
3. Chang, K. Topological insulating phase in commonly used semiconductors. *Natl. Sci. Rev.* **2014**, *1*, 34–35. [CrossRef]
4. Li, X.; Lu, H.; Li, R.; Wan, Z.; Wang, X.; Macis, S.; Lupi, S.; Gu, M.; Wang, H.; Yue, Z. Topological insulator materials for optics: Research progress and prospects. *Appl. Phys. Rev.* **2026**, *13*, 011301. [CrossRef]
5. Cai, S.; Guo, J.; Sidorov, V.A.; Zhou, Y.; Wang, H.; Lin, G.; Li, X.; Li, Y.; Yang, K.; Li, A.; et al. Independence of topological surface state and bulk conductance in three-dimensional topological insulators. *npj Quantum Mater.* **2018**, *3*, 62. [CrossRef]
6. Li, C.H.; van't Erve, O.M.J.; Robinson, J.T.; Liu, Y.; Li, L.; Jonker, B.T. Electrical detection of charge-current-induced spin polarization due to spin-momentum locking in Bi_2Se_3. *Nat. Nanotechnol.* **2014**, *9*, 218–224. [CrossRef]
7. Chen, P.; Chi, H.; Moodera, J.S. Progress and prospects of magnetic topological materials for spintronic applications. *Newton* **2026**, *2*, 100436. [CrossRef]
8. Wang, A.Q.; Ye, X.G.; Yu, D.P.; Liao, Z.M. Topological semimetal nanostructures: From properties to topotronics. *ACS Nano* **2020**, *14*, 3755–3778. [CrossRef]
9. Guo, Y.; Zhang, X.; Huang, Z.; Chen, J.; Luo, Z.; Zhang, J.; Li, J.; Zhang, Z.; Zhao, J.; Han, X.; et al. Quantum materials for spintronic applications. *npj Spintron.* **2024**, *2*, 36. [CrossRef]
10. He, Q.L.; Hughes, T.L.; Armitage, N.P.; Tokura, Y.; Wang, K.L. Topological spintronics and magnetoelectronics. *Nat. Mater.* **2022**, *21*, 15–23. [CrossRef]
11. Mithun, K.P.; Kumar, A.; Kundu, S.; Ravishankar, N.; Sood, A.K. Ultrafast dynamics of Dirac surface and bulk photocarriers in topological-insulator bismuth telluride nanocrystals using terahertz spectroscopy. *Phys. Rev. B* **2022**, *105*, 144302. [CrossRef]
12. Sim, S.; Lee, S.; Moon, J.; In, C.; Lee, J.; Noh, M.; Kim, J.; Jang, W.; Cha, S.; Seo, S.Y.; et al. Picosecond competing dynamics of apparent semiconducting-metallic phase transition in the topological insulator Bi_2Se_3. *ACS Photonics* **2020**, *7*, 759–764. [CrossRef]
13. Ruan, S.; Lin, X.; Chen, H.; Song, B.; Dai, Y.; Yan, X.; Jin, Z.; Ma, G.; Yao, J. Terahertz probe of nonequilibrium carrier dynamics and ultrafast photocurrents in the topological insulator Sb_2Te_3. *Appl. Phys. Lett.* **2021**, *118*, 011102. [CrossRef]
14. Wang, X.; Hou, T.; Yang, Z.; Li, S.; Jin, T.; Xiao, C.; Sofer, Z.; Qi, D.C.; Chang, G.; Wang, X.R. Unraveling scattering contributions to the nonlinear hall effect in topological insulator Bi_2Te_3. *Newton* **2026**, *2*, 100410. [CrossRef]
15. Chen, Y.L.; Analytis, J.G.; Chu, J.H.; Liu, Z.K.; Mo, S.K.; Qi, X.L.; Zhang, H.J.; Lu, D.H.; Dai, X.; Fang, Z.; et al. Experimental realization of a three-dimensional topological insulator, Bi_2Te_3. *Science* **2009**, *325*, 178–181. [CrossRef]
16. Zhang, H.; Liu, C.X.; Qi, X.L.; Dai, X.; Fang, Z.; Zhang, S.C. Topological insulators in Bi_2Se_3, Bi_2Te_3 and Sb_2Te_3 with a single Dirac cone on the surface. *Nat. Phys.* **2009**, *5*, 438–442. [CrossRef]
17. Zhang, H.; Zhang, X.; Liu, C.; Lee, S.T.; Jie, J. High-responsivity, high-detectivity, ultrafast topological insulator Bi_2Se_3/silicon heterostructure broadband photodetectors. *ACS Nano* **2016**, *10*, 5113–5122. [CrossRef]
18. Wang, X.B.; Cheng, L.; Wu, Y.; Zhu, D.P.; Wang, L.; Zhu, J.X.; Yang, H.; Chia, E.E.M. Topological-insulator-based terahertz modulator. *Sci. Rep.* **2017**, *7*, 13486. [CrossRef]
19. Giorgianni, F.; Chiadroni, E.; Rovere, A.; Cestelli-Guidi, M.; Perucchi, A.; Bellaveglia, M.; Castellano, M.; Di Giovenale, D.; Di Pirro, G.; Ferrario, M.; et al. Strong nonlinear terahertz response induced by Dirac surface states in Bi_2Se_3 topological insulator. *Nat. Commun.* **2016**, *7*, 11421. [CrossRef]
20. Zhang, X.; Wang, J.; Zhang, S.C. Topological insulators for high-performance terahertz to infrared applications. *Phys. Rev. B* **2010**, *82*, 245107. [CrossRef]
21. Sim, S.; Brahlek, M.; Koirala, N.; Cha, S.; Oh, S.; Choi, H. Ultrafast terahertz dynamics of hot Dirac-electron surface scattering in the topological insulator Bi_2Se_3. *Phys. Rev. B* **2014**, *89*, 165137. [CrossRef]
22. Jin, Z.; Hong, H.; Li, Z.; Peng, Y.; Zhu, Y.; Zhuang, S.; Sun, Y.; Li, J.; Peng, J.; Nie, T.; et al. Ultrafast All-Optical Terahertz Switchable Modulation Using Van Der Waals Fe_4GeTe_2/Bi_2Se_3 Heterostructures. *Adv. Opt. Mater.* **2025**, *13*, 2400951.
23. Cong, L.; Srivastava, Y.K.; Zhang, H.; Zhang, X.; Han, J.; Singh, R. All-optical active THz metasurfaces for ultrafast polarization switching and dynamic beam splitting. *Light Sci. Appl.* **2018**, *7*, 28. [CrossRef] [PubMed]
24. Kumar, A.; Solanki, A.; Manjappa, M.; Ramesh, S.; Srivastava, Y.K.; Agarwal, P.; Sum, T.C.; Singh, R. Excitons in 2D perovskites for ultrafast terahertz photonic devices. *Sci. Adv.* **2020**, *6*, eaax8821. [CrossRef]
25. Zeng, Y.; Wang, J.; Yang, X.; Yao, J.; Li, P.; He, Q.; Xu, M.; Miao, X. Broadband and ultrafast terahertz modulation with GeTe thin films. *Opt. Mater.* **2023**, *143*, 114188. [CrossRef]
26. Hajlaoui, M.; Papalazarou, E.; Mauchain, J.; Lantz, G.; Moisan, N.; Boschetto, D.; Jiang, Z.; Miotkowski, I.; Chen, Y.P.; Taleb-Ibrahimi, A.; et al. Ultrafast surface carrier dynamics in the topological insulator Bi_2Te_3. *Nano Lett.* **2012**, *12*, 3532–3536. [CrossRef]

27. Sobota, J.A.; Yang, S.; Analytis, J.G.; Chen, Y.L.; Fisher, I.R.; Kirchmann, P.S.; Shen, Z.X. Ultrafast optical excitation of a persistent surface-state population in the topological insulator Bi_2Se_3. *Phys. Rev. Lett.* **2012**, *108*, 117403. [CrossRef]
28. Kafle, T.R.; Zhang, Y.; Wang, Y.; Shi, X.; Li, N.; Sapkota, R.; Thurston, J.; You, W.; Gao, S.; Dong, Q.; et al. Non-equilibrium states and interactions in the topological insulator and topological crystalline insulator phases of $NaCd_4As_3$. *Struct. Dyn.* **2025**, *12*, 014501. [CrossRef]
29. Li, S.; Zhang, X.; Chen, H.Y.; Huang, C.W.; Huang, J.C.A.; Lee, C.K.; Chui, H.C. Ultrafast carrier dynamics in topological insulator thin films under ultralow excitation conditions. *Opt. Commun.* **2025**, *596*, 132438. [CrossRef]
30. Jabed, A.; Goto, F.; Frimpong, B.; Armanno, D.; Longa, A.; Michiardi, M.; Damascelli, A.; Hofmann, P.; Jargot, G.; Ibrahim, H.; et al. Control of intervalley scattering in Bi_2Te_3 via temperature-dependent band renormalization. *npj Quantum Mater.* **2026**, *11*, 5. [CrossRef]
31. Yun, T.; Chen, Z.; Lee, W.; Jiang, T.; Huang, D.; Wang, Z. Quantum control in 2D materials via ultrafast nonlinear optics. *Newton* **2026**, *2*, 1–7. [CrossRef]
32. Guo, Y.Y.; Chen, Z.Q.; Cai, M.; Jin, Z.M.; Wang, X.F.; Zhang, C.; Balakin, A.V.; Shkurinov, A.P.; Peng, Y.; Zhu, Y.M.; et al. Ultrafast Photogalvanic Effect in Ferromagnet/Dirac Semimetal Heterostructures Diagnosed by Terahertz Emission Spectroscopy. *ACS Photonics* **2026**, *13*, 1330–1342. [CrossRef]
33. Kamboj, V.S.; Singh, A.; Ferrus, T.; Beere, H.E.; Duffy, L.B.; Hesjedal, T.; Barnes, C.H.W.; Ritchie, D.A. Probing the topological surface state in Bi_2Se_3 thin films using temperature-dependent terahertz spectroscopy. *ACS Photonics* **2017**, *4*, 2711–2718. [CrossRef]
34. Qi, J.; Chen, X.; Yu, W.; Cadden-Zimansky, P.; Smirnov, D.; Tolk, N.H.; Miotkowski, I.; Cao, H.; Chen, Y.P.; Wu, Y.; et al. Ultrafast carrier and phonon dynamics in Bi_2Se_3 crystals. *Appl. Phys. Lett.* **2010**, *97*, 182102. [CrossRef]
35. Choi, Y.G.; Zhang, C.J.; Park, S.H.; Park, J.; Kim, J.S.; Kim, S.; Park, J.; Lee, J.S. Ultrafast transient photocarrier dynamics of the bulk-insulating topological insulator $Bi_{1.5}Sb_{0.5}Te_{1.7}Se_{1.3}$. *Phys. Rev. B* **2018**, *97*, 075307. [CrossRef]
36. Zhang, X.; Li, S.; Huang, C.W.; Huang, J.C.A.; Luo, C.W.; Lee, C.K.; Chui, H.C. A multi-state spectroscopic approach to carrier dynamics in thin-film topological insulators. *J. Mater. Chem. C* **2026**. [CrossRef]
37. Campanari, V.; Catone, D.; O'Keeffe, P.; Paladini, A.; Turchini, S.; Martelli, F.; Salvato, M.; Loudhaief, N.; Campagna, E.; Castrucci, P. Dynamics of the bulk-to-topological state scattering of photoexcited carriers in Bi_2Se_3 thin films. *ACS Appl. Electron. Mater.* **2023**, *5*, 4643–4649. [CrossRef]
38. Crepaldi, A.; Cilento, F.; Ressel, B.; Cacho, C.; Johannsen, J.C.; Zacchigna, M.; Berger, H.; Bugnon, P.; Grazioli, C.; Turcu, I.C.E.; et al. Evidence of reduced surface electron-phonon scattering in the conduction band of Bi_2Se_3 by nonequilibrium ARPES. *Phys. Rev. B* **2013**, *88*, 121404. [CrossRef]
39. Luo, C.W.; Wang, H.J.; Ku, S.A.; Chen, H.J.; Yeh, T.T.; Lin, J.Y.; Wu, K.H.; Juang, J.Y.; Young, B.L.; Kobayashi, T.; et al. Snapshots of Dirac fermions near the Dirac point in topological insulators. *Nano Lett.* **2013**, *13*, 5797–5802. [CrossRef]
40. Wang, Y.H.; Hsieh, D.; Sie, E.J.; Steinberg, H.; Gardner, D.R.; Lee, Y.S.; Jarillo-Herrero, P.; Gedik, N. Measurement of intrinsic Dirac fermion cooling on the surface of the topological insulator Bi_2Se_3 using time-resolved and angle-resolved photoemission spectroscopy. *Phys. Rev. Lett.* **2012**, *109*, 127401. [CrossRef]
41. Kikuchi, K.; Mizukoshi, Y.; Fukuda, T.; Fons, P.; Hase, M. Spin-dependent bandgap renormalization and state-filling effect in Bi_2Se_3 observed by ultrafast Kerr rotation. *Appl. Phys. Lett.* **2024**, *124*, 233104. [CrossRef]
42. Wang, X.; Lian, J.; Huang, Y.; Sun, Z.; Liu, J.; Zhang, F.; Gao, S.; Yu, X.; Li, P.; Zhao, M. Magneto-optical Faraday and Kerr effects in topological insulators Bi_2Te_3 and Bi_2Se_3. *Jpn. J. Appl. Phys.* **2013**, *52*, 103001. [CrossRef]
43. Kovalev, S.; Tielrooij, K.J.; Deinert, J.C.; Ilyakov, I.; Awari, N.; Chen, M.; Ponomaryov, A.; Bawatna, M.; de Oliveira, T.V.A.G.; Eng, L.M.; et al. Terahertz signatures of ultrafast Dirac fermion relaxation at the surface of topological insulators. *npj Quantum Mater.* **2021**, *6*, 84. [CrossRef]
44. Kuznetsov, K.A.; Tarasenko, S.A.; Kovaleva, P.M.; Kuznetsov, P.I.; Lavrukhin, D.V.; Goncharov, Y.G.; Ezhov, A.A.; Ponomarev, D.S.; Kitaeva, G.K. Topological insulator films for terahertz photonics. *Nanomaterials* **2022**, *12*, 3779. [CrossRef] [PubMed]
45. George, P.A.; Strait, J.; Dawlaty, J.; Shivaraman, S.; Chandrashekhar, M.; Rana, F.; Spencer, M.G. Ultrafast optical-pump terahertz-probe spectroscopy of the carrier relaxation and recombination dynamics in epitaxial graphene. *Nano Lett.* **2008**, *8*, 4248–4251. [CrossRef] [PubMed]
46. Zhou, J.; Zhou, T.; Yang, D.; Wang, Z.; Zhang, Z.; You, J.; Xu, Z.; Zheng, X.; Cheng, X. Optically Controlled Extraordinary Terahertz Transmission of Bi_2Se_3 Film Modulator. *Photonic Sens.* **2019**, *9*, 268–276. [CrossRef]
47. Choi, H.; Borondics, F.; Siegel, D.A.; Zhou, S.Y.; Martin, M.C.; Lanzara, A.; Kaindl, R.A. Broadband electromagnetic response and ultrafast dynamics of few-layer epitaxial graphene. *Appl. Phys. Lett.* **2009**, *94*, 172102. [CrossRef]
48. Strait, J.H.; Wang, H.; Shivaraman, S.; Shields, V.; Spencer, M.; Rana, F. Very slow cooling dynamics of photoexcited carriers in graphene observed by optical-pump terahertz-probe spectroscopy. *Nano Lett.* **2011**, *11*, 4902–4906. [CrossRef]

49. Luo, L.; Yang, X.; Liu, X.; Liu, Z.; Vaswani, C.; Cheng, D.; Mootz, M.; Zhao, X.; Yao, Y.; Wang, C.Z.; et al. Ultrafast manipulation of topologically enhanced surface transport driven by mid-infrared and terahertz pulses in Bi_2Se_3. *Nat. Commun.* **2019**, *10*, 607. [CrossRef]
50. Valdés Aguilar, R.; Qi, J.; Brahlek, M.; Bansal, N.; Azad, A.; Bowlan, J.; Oh, S.; Taylor, A.J.; Prasankumar, R.P.; Yarotski, D.A. Time-resolved terahertz dynamics in thin films of the topological insulator Bi_2Se_3. *Appl. Phys. Lett.* **2015**, *106*, 011901. [CrossRef]
51. Cocker, T.L.; Baillie, D.; Buruma, M.; Titova, L.V.; Sydora, R.D.; Marsiglio, F.; Hegmann, F.A. Microscopic origin of the Drude-Smith model. *Phys. Rev. B* **2017**, *96*, 205439. [CrossRef]
52. Park, B.C.; Kim, T.H.; Sim, K.I.; Kang, B.; Kim, J.W.; Cho, B.; Jeong, K.H.; Cho, M.H.; Kim, J.H. Terahertz single conductance quantum and topological phase transitions in topological insulator Bi_2Se_3 ultrathin films. *Nat. Commun.* **2015**, *6*, 6552. [CrossRef] [PubMed]
53. Jin, Z.; Peng, Y.; Fang, Y.; Ye, Z.; Fan, Z.; Liu, Z.; Bao, X.; Gao, H.; Ren, W.; Wu, J.; et al. Photoinduced large polaron transport and dynamics in organic-inorganic hybrid lead halide perovskite with terahertz probes. *Light Sci. Appl.* **2022**, *11*, 209. [CrossRef] [PubMed]
54. Jin, Z.; Gehrig, D.; Dyer-Smith, C.; Heilweil, E.J.; Laquai, F.; Bonn, M.; Turchinovich, D. Ultrafast terahertz photoconductivity of photoactive polymer–fullerene blends: A comparative study correlated with photovoltaic device performance. *J. Phys. Chem. Lett.* **2014**, *5*, 3662–3668. [CrossRef]
55. Purlu, K.M.; Dalgac, S.; Isik, E.; Yildiz, B.K.; Elmabruk, K. Strontium oxide-doped alumina-based functional ceramics: Microstructure, dielectric properties, and suitability for 5G/6G and millimeter-wave applications. *J. Mater. Sci. Mater. Electron.* **2026**, *37*, 322. [CrossRef]
56. Kar, S.; Mohapatra, D.R.; Freysz, E.; Sood, A.K. Tuning photoinduced terahertz conductivity in monolayer graphene: Optical-pump terahertz-probe spectroscopy. *Phys. Rev. B* **2014**, *90*, 165420. [CrossRef]
57. Kar, S.; Nguyen, V.L.; Mohapatra, D.R.; Lee, Y.H.; Sood, A.K. Ultrafast spectral photoresponse of bilayer graphene: Optical pump–terahertz probe spectroscopy. *ACS Nano* **2018**, *12*, 1785–1792. [CrossRef]
58. Suo, P.; Yan, S.; Pu, R.; Zhang, W.; Li, D.; Chen, J.; Fu, J.; Lin, X.; Miao, F.; Liang, S.J.; et al. Ultrafast photocarrier and coherent phonon dynamics in type-II Dirac semimetal $PtTe_2$ thin films probed by optical spectroscopy. *Photonics Res.* **2022**, *10*, 609–616. [CrossRef]
59. Guo, Y.; Chen, Z.; Jin, Z.; Wang, X.; Zhang, C.; Balakin, A.V.; Shkurinov, A.P.; Peng, Y.; Zhu, Y.; Zhuang, S. Dynamically controllable terahertz electromagnetic interference shielding by small polaron responses in Dirac semimetal $PdTe_2$ thin films. *Adv. Funct. Mater.* **2024**, *34*, 2407749. [CrossRef]

Disclaimer/Publisher's Note: The statements, opinions and data contained in all publications are solely those of the individual author(s) and contributor(s) and not of MDPI and/or the editor(s). MDPI and/or the editor(s) disclaim responsibility for any injury to people or property resulting from any ideas, methods, instructions or products referred to in the content.